Vibration sensor for particle concentration measurement in pneumatic pipeline flows

2010 Meas. Sci. Technol. 21 125401

(http://iopscience.iop.org/0957-0233/21/12/125401)

Meas. Sci. Technol. **21** (2010) 125401 (10pp) doi:10.1088/0957-0233/21/12/125401

Vibration sensor for particle concentration measurement in pneumatic pipeline flows

Brent M Meunier[1], Peter M Watts[1], Jeffrey S Marshall[1,3], Ronald L Dechene[2], Wei Du[2] and Robert E Newton[2]

[1] School of Engineering, The University of Vermont, Burlington, VT 05405, USA
[2] Auburn Systems, LLC, Danvers, MA 01923, USA

Received 13 July 2010, in final form 8 September 2010
Published 4 November 2010
Online at stacks.iop.org/MST/21/125401

Abstract
Accurate measurements of pneumatically driven particle mass flow rate and particle size are necessary in order to maintain optimal combustion efficiency in coal-fired power plants and cement manufacturing facilities, as well as numerous other operations which are fed by multiple particle injection ports. Existing sensors for pneumatic particle concentration, such as concentration sensors, are typically prohibitively expensive and their measurements are sensitive to particle moisture content. A new sensor was developed for particle concentration measurement in pneumatic pipeline flow based on measurement of particle effects on fluid-induced oscillations of a probe extending into the flow. Since fluid-induced oscillations occur at a much lower frequency than do particle collisions, the measurements can be made with much simpler and less expensive equipment than is the case with impact sensors that attempt to resolve individual particle collisions. Experimental tests indicate three statistical measures of the probe acceleration data that exhibit smooth variation with the particle diameter and concentration data. The experimental data are used to train a neural net, which serves to interpolate the data. It is found that by training the neural net data on the statistical measures of the sensor probe acceleration, information on the particle concentration field can be extracted with a reasonable degree of accuracy.

Keywords: particle concentration sensor, particle impact, neural net

Notation

Roman letters

$\tilde{a}^2$	power spectral density
a_{rms}	acceleration root mean square
d_i	diameter of a particle size i
D	probe diameter
f_{a}	accelerometer frequency
f_{zc}	acceleration zero-crossing frequency
f_T	characteristic frequency for turbulent eddy impact on the probe
f_v	vortex shedding frequency
H	pipe diameter
k	spring constant
ℓ	integral length scale of the turbulent flow
L	probe length
m_p	mass of one particle
$\dot{m}_p$	particle feed rate
M_i	mass of particles of size i in the mixture
$\dot{n}$	particle collision rate
q	turbulent kinetic energy (per unit mass)
$\dot{Q}_p$	particle volumetric flow rate ($=\dot{m}_p/\rho_p$)
Re_C	probe Reynolds number ($= DU/\nu$)
Re_F	pipe flow Reynolds number ($= HU/\nu$)
Re_{p}	particle Reynolds number
Sh	Strouhal number ($= f_v D/U$)
St	Stokes number (equation (4))
u_0	turbulent velocity fluctuation standard deviation
U_i	fluid velocity at setting i

[3] Author to whom any correspondence should be addressed.

Greek letters

- ε turbulence dissipation rate (per unit mass)
- ϕ particle concentration
- η Kolmogorov length scale of the turbulent flow
- λ Taylor microscale of the turbulent flow
- μ fluid viscosity
- ν fluid kinematic viscosity ($\equiv \mu/\rho$)
- ρ_p particle density

1. Introduction

Controlling a modern pulverized coal-fired boiler, furnace or kiln at, or near, maximum efficiency is an extraordinarily complex problem. To achieve efficient combustion requires consistent and balanced fuel distribution and optimum air-to-fuel mixtures. Uneven fuel distribution can cause unstable flame intensities and related safety issues and is one of the principle causes of burner inefficiency. Imbalanced fuel distribution can also result in local sub-optimal air-to-fuel ratios, thus increasing CO, NO_x and unburned fly ash carbon content of the exhaust. In the cement industry, an increased unburned carbon content directly degrades the quality of the cement produced. Unnecessary additional air flow will not only decrease valuable heat generation rate, but also create excessive NO_x emissions.

Various approaches have been used to measure mass flow rate, concentration and particle diameter in industrial gas–solid particulate flow processes. These approaches utilize ultrasound attenuation [1–6], radiometric methods based on beta- or gamma-ray absorption [7–9], electrical capacitance [10–15], light scattering [16], microwave backscatter [17–19], acoustic emissions and resonance [20, 21], magnetic resonance [22] and mechanical vibrations [23, 24]. Reviews of particle sensing approaches for pneumatic conveyance are given by Yan [25], Beck *et al* [26], Penner *et al* [27] and Ahmed and Ismail [28]. Monitoring and controlling the fuel delivery system with many current particle flow sensors is difficult due to requirements on sensor accuracy, durability and cost–benefit ratio. Also, some sensors based on electric field measurements, such as capacitance, are sensitive to particle moisture content [29], which is not often accurately known during system operation.

A number of sensor designs have recently been proposed which are based on measuring the vibrations caused by impact of particles either with a bend in the pipeline wall [30] or with an obstacle introduced into the pipeline flow [23, 24]. Impact sensors are often used in geophysical applications for measurement of particle motion near the ground. For instance, Rickenmann and McArdell [31] used a piezoelectric impact sensor to measure bedload sediment transport rate in a stream, and Schaer and Islar [32] used an impact sensor to measure the effective size, density and velocity of snow particle clusters in avalanches. Coghill [23, 24] designed an impact sensor for measurement of pneumatic particle transport. In this approach, particles collide with a rigid sensor arm that is held in the flow field, and the duration and amplitude of the acoustic pulse propagated on the sensor arm is measured. The Hertzian particle impact theory is then used to estimate the particle size and impact velocity [33], and the particle concentration is estimated from the collision frequency. This approach is most applicable for low concentrations, so that incidents of more than one particle impacting the sensor at any given time are rare, and for larger particles, so that particles are not substantially deflected by the air flow about the sensor.

The current paper describes a different approach to particle impact/vibration sensing in which the sensor probe is designed to oscillate slightly in the flow stream in response to both the flow oscillations and particle collisions. The flow oscillations are related both to vortex shedding from the probe and to impact onto the probe of upstream turbulent eddies. Statistical measures of the probe acceleration are identified which vary smoothly with changes in particle size and mass flow rate. A neural net is used to relate the statistical measures to the particle size and concentration field. The proposed approach has the advantage of being very simple and inexpensive, since it is constructed entirely of standard commercially available parts, while providing simultaneous measurement of particle concentration with reasonable accuracy once sufficient data are collected to train the neural net.

2. Methods and materials

2.1. Sensor design

The impact/vibration sensor is illustrated in figure 1. The impact surface consists of a cylindrical probe (diameter $D = 0.95$ cm) that extends a distance of $L = 2.8$ cm into the flow through a hole threaded into the pipe wall. The probe is supported by a pin located approximately at the inner surface of the pipe, about which the probe is free to pivot. The pin is attached to a straight nipple that is threaded into the pipe wall, so that the outer surface of the nipple is flush with the outer surface of the pipe wall. A flexible nylon bushing is positioned around the probe and the nipple at the same location as the pin in order to eliminate particle leakage into the sensor. The opposite end of the probe is attached to two compression springs (spring constant $k = 0.08$ N mm^{-1}), which are attached to rigid support bars within the sensor housing. At the outer end of the probe end (within the sensor housing) is attached an accelerometer (Analog Devices ADXL203, $\pm$ 2 g, 0–5000 Hz range), the data from which are fed to a DataQ data acquisition device and stored on a laptop computer.

2.2. Experimental tests

The impact-vibration sensor was tested in a two-phase, gas–solid, open flow loop at Auburn Systems. The main components of the flow loop, illustrated in figure 2, consist of an air inlet section with a fan to generate the air flow, a pitot tube flow meter, a particle hopper and feed rate control, a straight 3.1 m long test section of pipe (from the feeder to the sensor) with a diameter $H = 7.3$ cm and an outlet port. Experiments were conducted with five different values of the mean velocity within the test section, $U_1, \ldots, U_5$, and five different mean particles diameters, $d_1, \ldots, d_5$, listed in

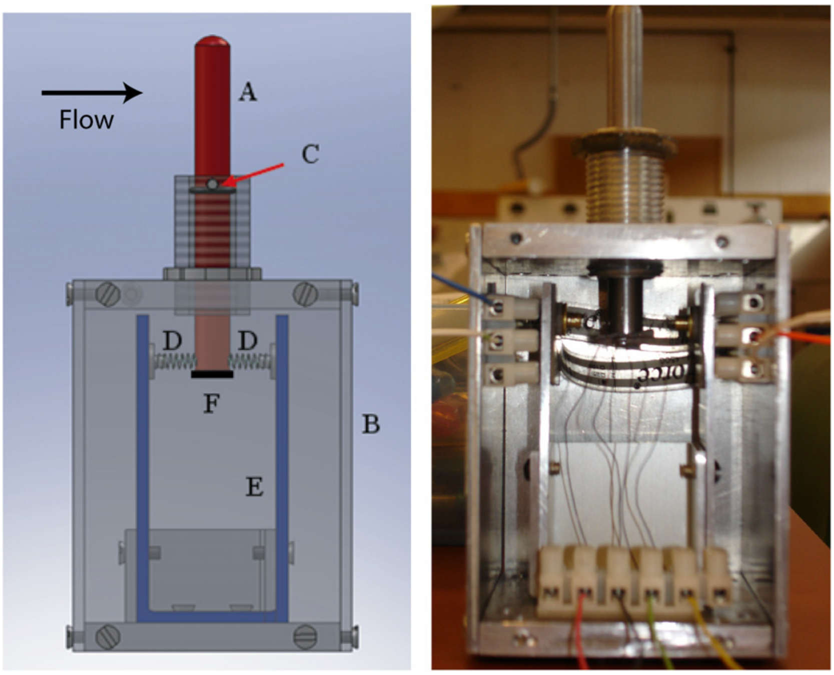

(*a*) (*b*)

Figure 1. (*a*) Schematic diagram and (*b*) photograph of the impact-vibration sensor, showing [A] probe, [B] housing, [C] pivot, [D] springs, [E] spring support and [F] accelerometer.
(This figure is in colour only in the electronic version)

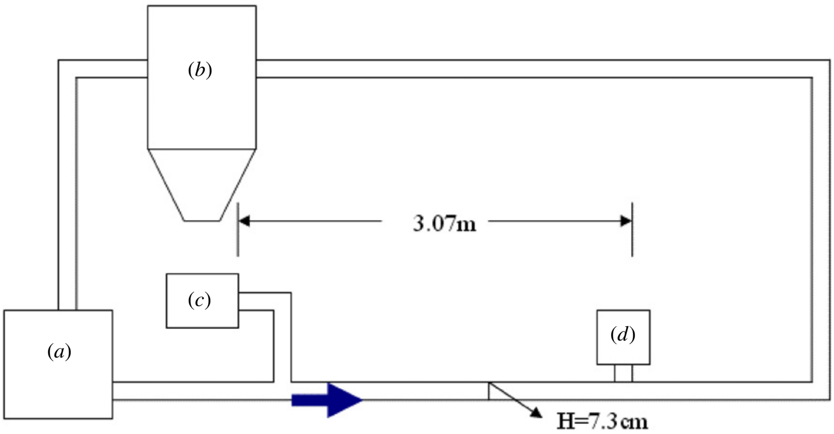

Figure 2. Schematic diagram of the Auburn system flow loop used for testing the sensor: (*a*) fan and motor, (*b*) fabric filter and dust collector, (*c*) particle feeder and (*d*) sensor placement.

table 1. The particles used in the experiment were glass beads obtained from Potters Industries, Inc., and consisted of three mesh sizes, 40–60 (325), 60–120 (188), and 170–325 (66 μm). The remaining two particle sizes were obtained by mixing the 40–60 and 60–120 mesh (256 μm) and by mixing the 60–120 and 170–325 mesh (129 μm), and the average particle diameters were obtained by weighing the amount of each mesh type added to each mixture and using the equation

$$d_3 = \frac{M_1}{M_1 + M_2} d_1 + \frac{M_2}{M_1 + M_2} d_2, \qquad (1)$$

where d is the average particle diameter, M is the mass of particles added to the mixture, subscripts 1 and 2 represent each mesh used, and subscript 3 represents the resultant mixture. The uncertainty in the flow velocity listed in table 1 represents the standard deviation of the velocity readings under constant experimental conditions. The

Table 1. Values of velocity and mean particle diameter used in the experiments.

Parameter number, i	Velocity, U_i (m s^{-1})	Mean particle diameter, d_i (μm)
1	10.2 ± 0.51	66 ± 22
2	15.2 ± 0.51	129 ± 43
3	20.3 ± 1.02	188 ± 63
4	25.4 ± 1.02	256 ± 69
5	30.5 ± 1.02	325 ± 75

uncertainty in the particle diameter listed in table 1 was determined by the upper and lower mesh sizes used for straining each particle size class, such that the particle diameter varies between these limits with uniform probability.

The particle feed rates used in the experiments were set through the use of a dc screw feeder which could vary the volumetric rate at which particles left the feeder by a 0–100% control knob that directly adjusts the speed of the motor. The experiments were conducted with particle feed rates $\dot{m}_p$ ranging from 0.008 to 0.06 kg s^{-1}. The feed rates were determined by measuring how much time it took for a measured mass of particles to flow out of the feeder. The uncertainty in the mass flow rate has an average value of $\pm 0.000\,23$ kg s^{-1}, which was determined via a multivariate propagation of error equation of the form

$$\Delta \dot{m}_p = \sqrt{(\Delta M_i)^2 (1/t)^2 + (\Delta t)^2 (-M_i/t^2)^2}, \qquad (2)$$

where M_i is the mass of particles of type i, t is the time interval and Δ denotes the uncertainty of the given variable. The particle mass and time measurement uncertainties are estimated to be $\Delta M_i = 2.3 \times 10^{-4}$ kg and $\Delta t = 0.1$ s, respectively. The particle concentration ϕ was determined by assuming that the average fluid and particle velocities are equal, and then taking the ratio of the particle volumetric flow rate to the total volumetric flow rate, giving

$$\phi = \frac{\dot{Q}_p}{(\pi/4)H^2 U + \dot{Q}_p}, \qquad (3)$$

where $\dot{Q}_p = \dot{m}_p/\rho_p$ is the particle volumetric flow rate.

2.3. Sensor analysis

Particles impacting on the cylindrical probe impart an impulsive force on the probe that is proportional to the particle impact velocity. The impact velocity is a function of both the upstream flow speed and the particle Stokes number *St*, defined as the ratio of the particle response time to the characteristic time scale of the fluid flow, where the latter is typically set equal to the ratio of the pipe diameter H and the mean fluid velocity U. The Stokes number is then given by

$$St = \rho_p d^2 U / 18 \mu H, \qquad (4)$$

where ρ_p are the particle density and μ is the fluid viscosity. For large values of *St*, the particle inertia is much greater than the fluid drag force, so that particles impact the cylinder with a velocity on the same order of magnitude as the fluid velocity U. For $St \ll 1$, the particle inertia is small compared to fluid drag force and particles approximately travel with the fluid streamlines, plus a small drift velocity of $O(StU)$. (A detailed derivation of this result can be obtained from a scaling argument using the particle inertia and fluid drag terms of the particle momentum equation, as presented in the book by Crowe *et al* [34].) For the experimental test conditions used in this study, the Stokes number varies between 4 and 330, so we may assume that the particles were only moderately influenced by the fluid flow around the probe. For a particle flow with concentration ϕ carried past a cylindrical probe with a frontal area DL, the average particle collision rate $\dot{n}$ on the probe is therefore given by [35]

$$\dot{n} = \frac{\rho_p DL}{m_p} U \phi, \qquad (5)$$

where $m_p = (\pi/6)\rho_p d^3$ is the particle mass. The collision rate ranges from 1.3×10^4 to 6.8×10^6 Hz for the particles used in the current study.

In addition to probe oscillations caused by collisions with individual particles, the probe also responds to fluid-induced oscillations caused by periodic vortex shedding from the probe. The probe Reynolds number $Re_C = DU/\nu$ varies from 6100 to 18 400 in our experiments, so the probe flow field is laminar with a vortex shedding Strouhal number $Sh = f_v D/U$ of approximately 0.2, where f_v is the vortex shedding frequency [36]. For the experimental conditions examined in this study, this Strouhal number corresponds to a vortex shedding frequency of between 210 and 640 Hz. The probe lift force oscillates at the vortex shedding frequency and the drag force oscillates at a frequency f_d equal to twice the vortex shedding frequency [36]. Lashkov [35], in a study of the effect of micron-size particles on the drag force acting on a cylinder, reports that particles can induce early onset of turbulence in the cylinder wake, thereby decreasing the critical Reynolds number for drag crisis. There appears to have been no detailed study to date of the effect of particles on the vortex shedding from the cylinder.

In addition to the vortices shed from the cylinder, the probe experiences collisions with upstream vortices in the turbulent pipe flow. The pipe flow Reynolds number $Re_F = HU/\nu$ averages approximately 94 120 for our experiments, so the pipe flow is clearly turbulent. The flow turbulent kinetic energy $q = 3u_0^2/2$, where u_0 is the root-mean-square fluctuation velocity, and the dissipation rate ε can be used to characterize the length scales of the turbulent flow. (In accord with usual usage, q is expressed as energy per unit mass and ε is expressed as energy per unit mass per unit time.) Three primary measures of length scale exist for turbulent flows—the Kolmogorov scale η, the Taylor microscale λ and the integral scale ℓ are defined by

$$\eta = (\nu^3/\varepsilon)^{1/4}, \qquad \lambda = (15\nu/\varepsilon)^{1/2} u_0, \qquad \ell = 0.5 u_0^3/\varepsilon. \qquad (6)$$

The Kolmogorov scale is the characteristic scale at which eddies decay due to viscous dissipation, the Taylor microscale is characteristic of the inertial range eddies, and the integral length scale is characteristic of the large, energy-containing eddies. Turbulence quantities for single and two-phase flows are measured by Tsuji *et al* [37] and Bohnet and Triesch [38] for pipe flow with a similar Reynolds number and diameter to that reported in the current experiments. These studies found that the ratio u_0/U varies between 0.05 and 0.1 for pipe turbulence, giving on average $q \cong 0.008U^2$. Tsuji *et al* [37] report values for the Taylor scale and the Kolmogorov scale as 1.5 and 0.1 mm, respectively, for a case with no particles at the center of the pipe. Using the definitions of the three length scales, the integral length can be expressed as a function of the other two length scales as

$$\ell = \frac{1}{30\sqrt{15}} \frac{\lambda^3}{\eta^2}, \tag{7}$$

so that the corresponding integral length scale is $\ell = 2.9$ mm. The characteristic frequency for large eddy impact with the probe is therefore approximately $f_T = U/\ell$, which using the data of Tsuji *et al* [37] to estimate the integral length scale and the average velocity of 20 m s^{-1} yields a large eddy collision frequency of about 6900 Hz.

The inclusion of particles in the fluid can influence the turbulence of the flow, thus altering the different turbulence-induced effects, such as eddy impact frequency. While not all of the relationships between the inclusion of particles and turbulence are understood at this time, the inclusion of particles with $Re_p > 400$, where Re_p is the particle Reynolds number, will increase the turbulence of the fluid due to particle-induced vortex shedding [39]. While large particles typically enhance the fluid turbulence, small particles will attenuate the affects of turbulence. The distinction between the two is determined by the ratio of the particle diameter to the turbulence integral length scale ℓ, such that for $d/\ell < 0.1$ the turbulence is attenuated by the particles [40]. A review of recent research on effects of particles on turbulent pipe flow is given by Bohnet and Triesch [38]. Assuming that the particle relative velocity is of the same order of magnitude as the average air velocity, the particle Reynolds number varies from about 40 to 630 for the current experiments, and the ratio d/ℓ varies between 0.023 and 0.11. Hence, the smallest size particles ($d = 66$ μm) are clearly in the range that we would expect attenuation of the turbulence by the particles and the largest size particles ($d = 325$ μm) are close to the dividing point between turbulence attenuation and enhancement.

It is also well known that turbulence can induce particles to be thrown out of the turbulent eddies by centrifugal action and to collect in thin, high-density sheets in-between eddies. Numerical simulations by Squires and Eaton [41] for homogeneous turbulence demonstrate that the local particle concentration can increase via this mechanism to over 25 times the mean concentration. Thus, even if the particle mean concentration is low enough that it does not substantially influence the turbulence, the magnitude of the turbulent-induced vibrations on the probe could be substantially increased due to impact of high-concentration particle clusters onto the probe, at a frequency approximately equal to the large-eddy impact frequency f_T.

It is evident from the above discussion that the probe is subject to forcing oscillations over a broad range of frequencies due to a variety of mechanisms. Resolution of the highest frequency forcing, caused by collisions of the probe with individual particles, requires very high temporal resolution, making such systems expensive and data intensive. On the other hand, the fluid-induced oscillations arising both from vortex shedding from the probe and from impact of upstream turbulent eddies with the probe occur at much lower frequencies, in the range of 400–7000 Hz and can be measured using a standard accelerometer. Whereas previous impact sensors are based on resolution of individual particle impact [23, 24], the sensor used in the current study seeks instead to determine the particle flow properties indirectly by examining the effect of particle diameter and concentration on the much slower fluid-induced oscillations of the probe.

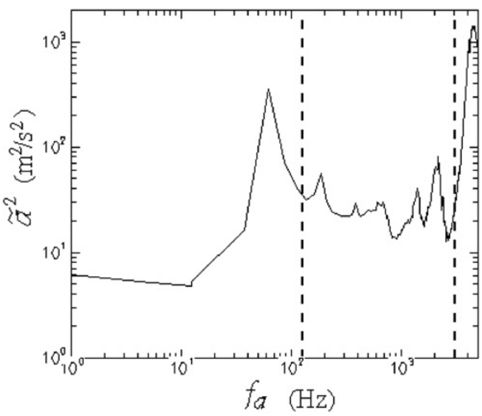

Figure 3. Power spectra of the acceleration field for $d = 325$ μm particles transported through a flow loop with a particle concentration of $\phi = 0.0456$ for $U = 30.5$ m s^{-1}. Due to the limited number of data points for low frequencies, the lack of complete data for the spike at around 4000 Hz, and the fact that the spike at around 70 Hz is not particle dependent, all frequency plots and average power spectral density values are determined only for the ranges of 125 to 3000 Hz as represented by the dashed lines in the figure.

3. Results and discussion

3.1. Statistical measures

Probe acceleration is measured as a function of time, and statistical measures of the acceleration data are computed using Matlab. The computed measures include root mean square, skewness and zero-crossing frequency of the acceleration signal. The power spectrum of the acceleration is computed, and additional statistical measures include maximum and average values of the power spectral density function.

While the accelerometer used to collect the experimental data provided a bandwidth of 0–5000 Hz, the power spectra plots and the average values of the power spectral density are determined only for the accelerometer frequency, f_a, range of 125–3000 Hz. This range was determined, as illustrated in figure 3, with respect to three observable phenomena in the logarithmically scaled power spectra plots. The first involved the inaccuracy of results for frequencies below 25 Hz due to the limited number of data points. The second regarded the lack of complete data for an observable spike in the plots at around 4000 Hz. While this frequency response illustrated a very distinct trend with respect to changes in particle size and concentration, it was omitted from further data analysis due to a portion of the response being at a frequency greater than the upper limit of the accelerometer bandwidth thus not providing a complete representation of the response effect. The third consisted of a spike in the plots at around 70 Hz which is not particle dependent, but is instead related to the natural frequency of the probe oscillations. Because this response was

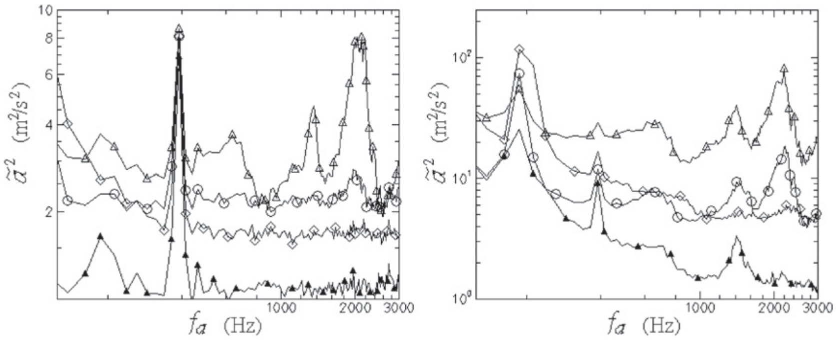

(*a*) (*b*)

Figure 4. Power spectra of the acceleration field for no particles (solid triangle) and for $d = 66$ μm (diamond), $d = 188$ μm (circle), and $d = 325$ μm (triangle) particles with an average particle concentration of $\phi = 0.0422$: (*a*) $U = 10.2$ m s^{-1} and (*b*) $U = 30.5$ m s^{-1}.

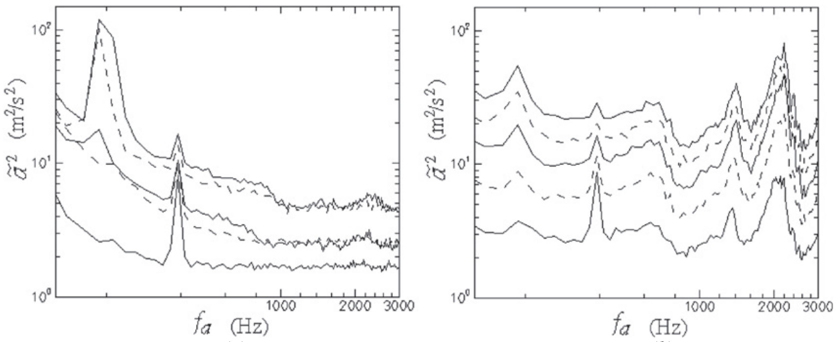

(*a*) (*b*)

Figure 5. Power spectra of the acceleration field with respect to different fluid velocities; starting at the base of the plots and moving to the top, $U = 10.2$ m s^{-1} (solid), $U = 15.2$ m s^{-1} (dashed), $U = 20.3$ m s^{-1} (solid), $U = 25.4$ m s^{-1} (dashed) and $U = 30.5$ m s^{-1} (solid); for flows consisting of an average particle concentration of $\phi = 0.0422$: (*a*) $d = 66$ μm and (*b*) $d = 325$ μm.

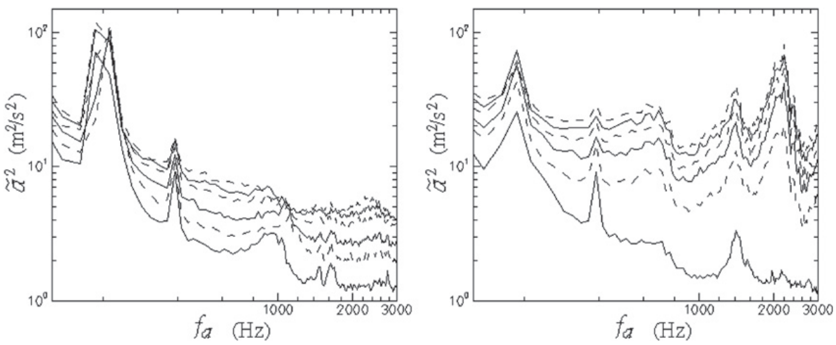

(*a*) (*b*)

Figure 6. Power spectra of the acceleration field with respect to different particle concentrations; starting at the base of the plots and moving to the top, $\phi = 0.0$ (solid), $\phi = 0.0086$ (dashed), $\phi = 0.0172$ (solid), $\phi = 0.0258$ (dashed), $\phi = 0.0345$ (solid) and $\phi = 0.0422$ (dashed); for $U = 30.5$ m s^{-1}: (*a*) $d = 66$ μm and (*b*) $d = 325$ μm.

not particle-dependent and had a value of the power spectral density, $\tilde{a}^2$, approximately ten times larger than the remaining power spectra values, it was omitted from further analysis. The statistical and neural net analyses reported in the paper have been repeated with different ranges in the spectral plots, including the entire range $f > 125$ Hz, and the qualitative results of the paper do not differ significantly.

Examples of the power spectra plots with respect to changes in particle diameter, fluid velocity and particle concentration are given in figures 4–6, respectively. As can be seen from the plots, the $\tilde{a}^2$ values increase with either an increase in fluid velocity or an increase in concentration and, with a few exceptions, the values generally increase with an increase in particle diameter. For low fluid velocities, the $\tilde{a}^2$ values increase over a majority of the frequency range with respect to an increase in particle diameter; however, at larger fluid velocities the values tend to overlap at different frequencies, such that an increase in particle diameter may or may not increase the $\tilde{a}^2$ value. Two notable observations in the power spectra plots with respect to particle diameters occur at the approximate frequency values of 200 and 2000 Hz. For fluid velocities above 25 m s^{-1}, it is observed that the $\tilde{a}^2$ values decrease with an increase in particle size at 200 Hz while at velocities below 25 m s^{-1} the values are

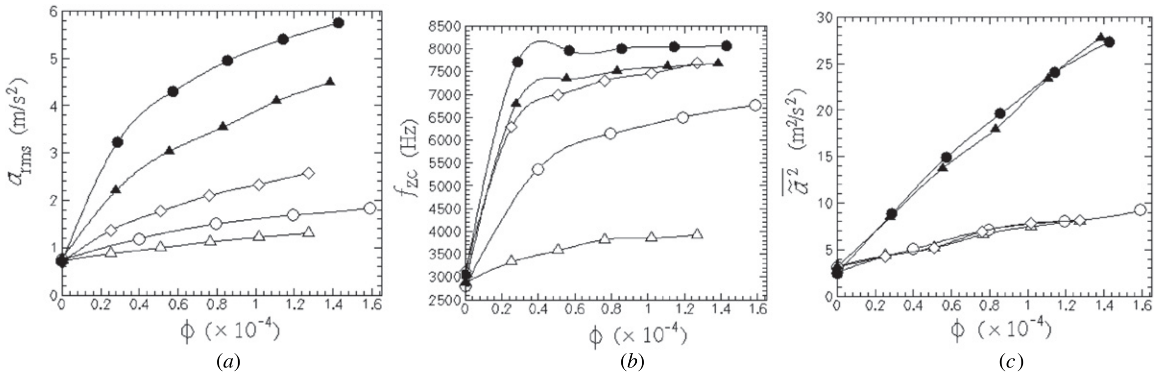

Figure 7. Plots showing variation of (*a*) acceleration root mean square, (*b*) acceleration zero-crossing frequency, and (*c*) average power spectral density with particle concentration for $d = 66\ \mu$m (triangle), $d = 129\ \mu$m (circle), $d = 188\ \mu$m (diamond), $d = 256\ \mu$m (solid triangle) and $d = 325\ \mu$m (solid circle), for experiments with $U = 30.5$ m s^{-1}.

nearly the same. At 2000 Hz, a frequency response that is directly related to an increase in particle diameter is observed within the range of fluid velocities used in this study.

The skewness and maximum power spectral density exhibited significant fluctuations with variation in particle diameter and concentration, and hence were not used for further data analysis. However, the acceleration root mean square (a_{rms}), zero-crossing frequency (f_{zc}) and average power spectral density ($\overline{\tilde{a}^2}$) all exhibit smooth variation with particle diameter, concentration change or both. The plots showing variation of these three statistical measures as a function of particle concentration are given in figure 7 for different particle sizes and mean transport velocity $U = 30.5$ m s^{-1}. The plots with other velocity values appear qualitatively similar. All three of these measures are observed to increase with an increase in flow velocity, particle concentration and particle diameter in nearly all cases examined; however, the rate of increase is not linear and there are some exceptions. For instance, experiments with the smallest particle diameter exhibit very little change in root-mean-square acceleration as the particle concentration is increased, whereas the experiments with the largest size particles exhibit a substantial increase in this parameter with an increase in the concentration. On the other hand, the largest particles exhibit very little change in zero-crossing frequency with concentration variation, whereas the smaller particles exhibit a larger increase in this measure with an increase in the concentration; an exception of this includes the change of decreasing to increasing values, with respect to an increase in the concentration, for 66 μm particles as the fluid velocity increases. We also observed that the two largest and the three smallest particle sizes have nearly the same value of the average power spectral density; however, the larger particles have a much larger value of this measure at the same concentration. A significant change in values of the zero-crossing frequency between the largest and smallest particles is also noticeable from these plots.

3.2. *Neural net data interpolation*

Since the process by which particles modify the fluid flow about the probe is complex, it is difficult to analytically determine the dependence of the various statistical measures on the particle size, velocity and concentration. For this reason, a neural net is used to predict the concentration from data for the three statistical measures of the sensor acceleration output, where it is assumed that the fluid mean velocity U is known by separate measurement of the air intake rate. In the current work, we used commercial neural net software called NeuroXL Predictor for this purpose. The neural network is trained using a zero-based log-sigmoid activation function and the experimental data for particle concentration, diameter, air velocity and the three statistical measures shown in figure 7. Given sufficient data on the effect of particle parameters on these statistical measures to train the network, the neural net can be used to predict the particle concentration field from the given air flow velocity and the measured values of the acceleration root mean square, zero-crossing frequency and average power spectral density function obtained from the sensor output. The process used for neural net prediction of the particle concentration is illustrated in the flow chart in figure 8.

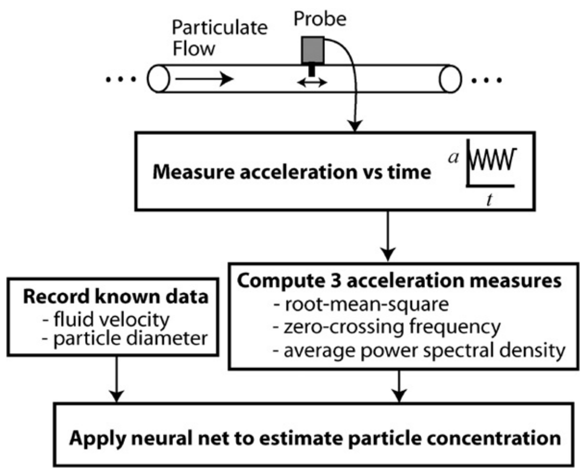

Figure 8. Flow chart illustrating use of a neural net to measure particle concentration with known fluid velocity and particle diameter.

A plot is shown in figure 9 demonstrating the ability of the neural net to reproduce the same data for which it is trained. All of the experimentally measured data for particle diameter,

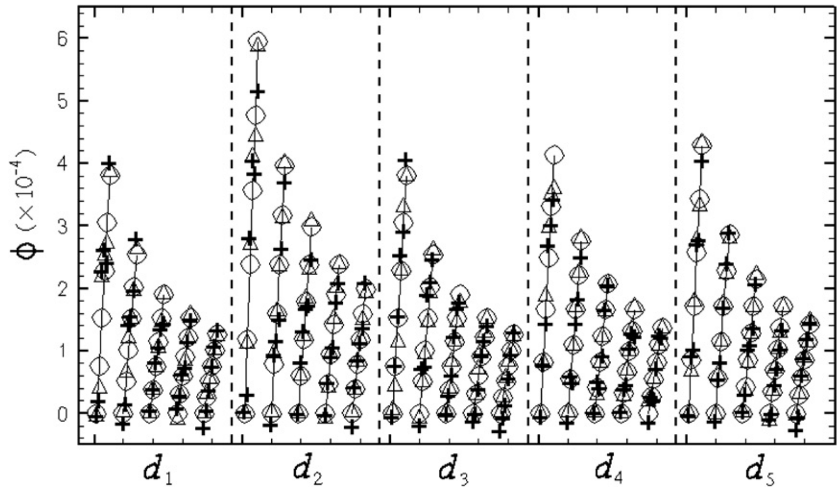

Figure 9. Neural net predictions for particle concentration for set A (triangles) and set B (plus signs) are plotted with respect to the original experimental data (circles). Dotted lines separate the results for each particle size. Each line represents the mean fluid velocity used to obtain that set of data, with velocity U_1 on the left progressing through velocity U_5 on the right for each particle size section.

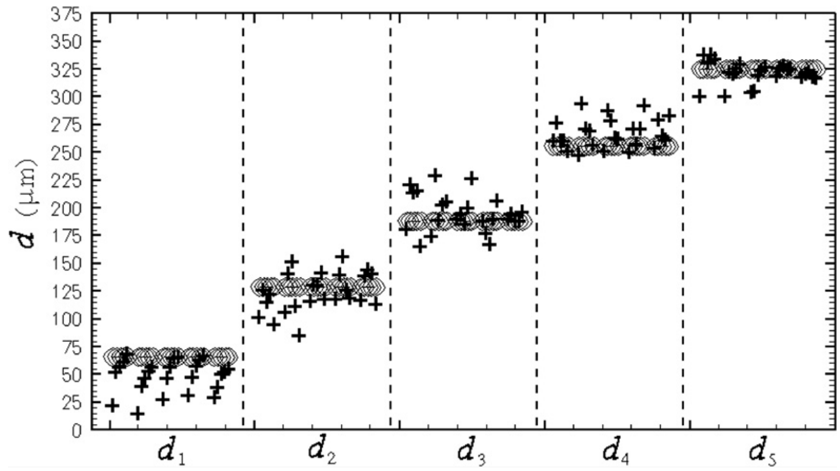

Figure 10. Neural net predictions for particle diameter for set B (plus signs) are plotted with respect to the original experimental data (circles). The lines have the same meaning as in figure 9.

concentration, fluid velocity and the three statistical measures discussed earlier in this section are used to train the neural net. Once trained, the neural net is then asked to predict certain *output* quantities from this same data set based on the value of a set of *input* quantities. Two sets of predictions are performed in this study. In set A, only the particle concentration is used as an output variable and the particle diameter, fluid velocity and the three statistical measures are all used as input variables. In set B, both the particle concentration and diameter are used as output variables and the input variables are the fluid velocity and the three statistical measures. The differences between the measured concentration values and these two prediction approaches are indicated by the different symbols in figure 9. As can be seen in the plot, both approaches produce results that match reasonably well with the experimental data, but in general the set A predictions are more accurate than the set B predictions. Figure 10 shows the particle diameter results from the set B predictions in comparison to the measured values from the experiments. While the predictions in this case exhibit greater variation than for the concentration predictions, particularly for small particle diameters, it is noted that the experimental uncertainty in the particle diameter is also quite large, averaging about one third of the mean particle diameter.

In order to assess the accuracy of the neural net in predicting data that are different from that for which it is trained, a second set of tests were conducted in which the neural net was trained only for data for particles sizes d_1, d_3 and d_5, and then used to predict the results for particle sizes d_2 and d_4. Again, predictions were made with only concentration as an output (set A) and with both concentration and particle size as outputs (set B). A comparison between the results of these two sets of predictions with the experimental data is shown in figure 11. Both prediction approaches tend to under-predict the concentration values for particle size d_2, although set A results are better than those from set B. The set A predictions for particle size d_4 agree well with the data, but the set B predictions again exhibit substantial deviation.

The sensitivity in the neural net predictions to data uncertainty was estimated by evaluating the standard deviation

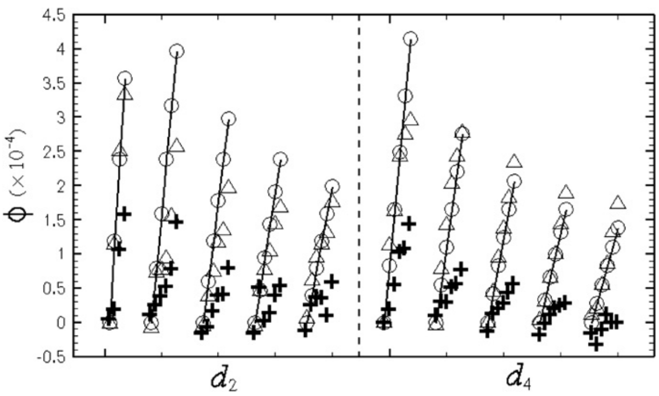

Figure 11. Neural net predictions for particle concentration for set A (triangles) and set B (plus signs) are plotted with respect to the original experimental data (circles). The lines have the same meaning as in figure 9. For this figure, only the data for particle sizes d_1, d_3 and d_5 are used to train the neural net and predictions are reported for sizes d_2 and d_4.

in the statistical measures obtained from the sensor data. Upper and lower bounds in the neural net prediction are determined by considering cases where the three statistical measures are perturbed by an amount equal to their measured value plus their measurement uncertainty, as well as their measured value minus their uncertainty, and for each case the neural net prediction was determined. These predictions were then subtracted from the original interpolated results and averaged in order to determine the uncertainty range of the neural net predictions. For the set A and set B predictions, the average variation between the upper and lower bound values in the neural net particle concentration prediction is 2.78×10^{-5} and 1.16×10^{-4}, respectively. These values are approximately an order of magnitude larger than the standard deviation of the experimentally measured values of the particle concentration, which has an average value of approximately 7.83×10^{-6}.

4. Conclusions

An inexpensive vibration sensor has been developed for prediction of particle concentration in pneumatic gas–solid particulate pipeline flow. The sensor consists of a cylindrical probe extending orthogonally into the flow, which is hinged about a pin at the position of the pipe wall. The opposite end of the probe is attached to two compression springs, allowing it to vibrate slightly, and acceleration data from the probe tip are collected. Three statistical measures of the probe acceleration field are found to vary smoothly with the particle size, velocity and concentration fields—the acceleration root mean square, the zero-crossing frequency and the average power spectral density. The power spectral density is clipped in frequency space to provide an estimate of the signal 'energy' in a frequency interval in which significant variation is observed with particle concentration change. These measures generally tend to increase in value as the particle size, concentration and velocity increase, indicating higher amplitude and more rapid fluctuation of the probe. A neural net system is trained on the data obtained from the vibration sensor and is found to be reasonably accurate for interpolating the data set. Specifically, when measures of the three statistical measures, the flow velocity and the particle size are input into the neural net, the system yields predictions for particle concentration that agree with reasonable accuracy to the experimental data, both for predicting the data used to train the system and for interpolating data lying in-between that used to train the system. Predictions of both particle concentration and size as an output produced reasonable, but not as accurate, results when reproducing the same data used to train the neural net and poor results predicting data not used to train the neural net. In general, the accuracy of the neural net prediction will increase as more data are included in the training set.

The proposed system can be made entirely from inexpensive, commercially available parts. We do not attempt to resolve individual particle impacts on the probe, but instead base the measurements on the much lower-frequency oscillations of the probe–spring system, which are caused both by the fluid-induced oscillating forces on the probe and from the collective particle impact. Since the probe fluctuations arise, at least in part, from the fluid flow fluctuations, including those from the upstream turbulence incident upon the probe, it is not clear what the effects of the pipeline upstream conditions on the sensor performance are, if any. Hence, without further testing it is not clear whether the data used for training the neural net can be obtained at a place of sensor manufacture, or whether these data must be taken *in situ* at the location where the sensor will be used. In either case, the proposed sensor is much simpler and less expensive than existing sensors for pneumatic particle concentration field. These sensors are well suited to applications in which a large number of sensors are required, such as in balancing the many different fuel pneumatic feed lines for a pulverized coal combustion process.

Acknowledgments

This work was supported by Auburn Systems, LLC, and by the Senior Experience in Engineering Design (SEED) Program at the University of Vermont. Financial support was also provided by the US Department of Transportation (grant number DTOS59-06-G-00048).

References

[1] Brown G J, Reilly D and Mills D 1996 Development of an ultrasonic tomography system for application in pneumatic conveying *Meas. Sci. Technol.* **7** 396–405

[2] Lynnworth L C 1981 Ultrasonic flowmeters *Trans. Inst. Meas. Control* **3** 217–23

[3] Sanderson M L and Yeung H 2002 Guidelines for the use of ultrasonic non-invasive metering techniques *Flow Meas. Instrum.* **13** 125–42

[4] Sowerby B D, Millen M J, Abernethy D A and Wagner S 1991 On-line determination of pulversized coal mass flow using an ultrasonic technique *Ultrasonics Symp. (Orlando, FL, USA)* pp 953–6

[5] Millen M J, Sowerby B D, Coghill P J, Tickner J R, Kingsley R and Grima C 2000 Plant tests of an on-line multiple-pipe pulverised coal mass flow measuring system *Flow Meas. Instrum.* **11** 153–8

[6] Sheen S H and Raptis A C 1985 Active ultrasonic cross-correlation flowmeters for mixed-phase pipe flows *ISA Trans.* **24** 53–8
[7] Barratt I R, Yan Y, Byrne B and Bradley M S A 2000 Mass flow measurement of pneumatically conveyed solids using radiometric sensors *Flow Meas. Instrum.* **11** 223–35
[8] Mennell J, Byrne B and Yan Y 2000 Appraisal of radiometric techniques to determine absolute solids fraction in pneumatic suspensions of particulate solids *Flow Meas. Instrum.* **11** 213–21
[9] Yan Y, Byrne B and Coulthard J 1994 Radiometric determination of dilute inhomogeneous solids loading in pneumatic conveying systems *Meas. Sci. Technol.* **5** 110–19
[10] Abouelwafa M S A and Kendall E J M 1980 The use of capacitance sensors for phase percentage determination in multiphase pipelines *IEEE Trans. Instrum. Meas.* **IM-29** 24–7
[11] Beck M S, Green R G, Plaskowski A B and Stott A L 1990 Capacitance measurement applied to a pneumatic conveyer with very low solids loading *Meas. Sci. Technol.* **1** 561–4
[12] Sun M, Liu S, Lei J and Li Z 2008 Mass flow measurement of pneumatically conveying solids using electrical capacitance tomography *Meas. Sci. Technol.* **19** 045503
[13] Hu H L, Xu T M, Hui S E and Zhou Q L 2006 A novel capacitive system for the concentration measurement of pneumatically conveyed pulverized fuel at power stations *Flow Meas. Instrum.* **17** 87–92
[14] Irons G A and Chang J S 1983 Particle fraction and velocity measurement in gas-powder streams by capacitance transducers *Int. J. Multiph. Flow* **9** 289–97
[15] Xie C G, Stott A L, Plaskowski A and Beck M S 1990 Design of capacitance electrodes for concentration measurement of two-phase flow *Meas. Sci. Technol.* **1** 65–78
[16] Lu Q, Wang S M and Zhang X F 1988 An experimental study of measurement of particle volume concentration by light-scattering technique *Proc. 1st Int. Conf. on Measurement and Control of Granular Materials (Shenyang, People's Republic China)* pp 114–17
[17] Harris J 1972 Flow measurement using microwave radar techniques *Powder Technol.* **6** 85–9
[18] Hrin G P and Tuma D T 1977 Doppler microwave cavity monitor for particulate loading *IEEE Trans. Instrum. Meas.* **IM-26** 13–7
[19] Kobyashi S and Miyahara S 1984 Development of microwave powder flowmeter *Instrumentation (Japan)* **27** 68–73
[20] Buttle D J and Scruby C B 1990 Characteristics of particle impact by quantitative acoustic emission *Wear* **37** 63–90
[21] Vetter A A and Culick F E C 1987 Acoustical resonance measurement of particle loading in gas-solids flow *J. Eng. Gas Turbines Power* **109** 331–5
[22] King J D and Rollwitz W L 1983 Magnetic resonance measurement of flowing coal *ISA Trans.* **22** 69–76
[23] Coghill P J 2001 Particle size by impact measurement in pneumatically conveyed solids *Part. Part. Syst. Charact.* **18** 114–9
[24] Coghill P J 2007 Particle size of pneumatically conveyed powders measured using impact duration *Part. Part. Syst. Charact.* **24** 464–9
[25] Yan Y 1996 Mass flow measurement of bulk solids in pneumatic pipelines *Meas. Sci. Technol.* **7** 1687–706
[26] Beck M S, Green R G and Thorn R 1987 Non-intrusive measurement of solids mass flow in pneumatic conveying *J. Phys. E: Sci. Instrum.* **20** 835–40
[27] Penner S S, Wang C P and Bahadori M Y 1984 Nonintrusive diagnostic techniques for measurements on coal-combustion systems *Prog. Energy Combust. Sci.* **10** 209–12
[28] Ahmed W H and Ismail B I 2008 Innovative techniques for two-phase flow measurements *Recent Patents Electr. Eng.* **1** 1–13
[29] Curtis J O 2001 Moisture effects on the dielectric properties of soils *IEEE Trans. Geosci. Remote Sens.* **39** 125–8
[30] Tallon S J and Davies C E 2000 The effect of pipeline location on acoustic measurement of gas–solid pipeline flow *Flow Meas. Instrum.* **11** 165–9
[31] Rickenmann D and McArdell B W 2007 Continuous measurement of sediment transport in the Erlenbach stream using piezoelectric bedload impact sensors *Earth Surf. Process. Landf.* **32** 1362–78
[32] Schaer M and Islar D 2001 Particle densities, velocities and size distributions in large avalanches from impact sensor measurements *Ann. Glaciol.* **32** 321–7
[33] Hertz H 1882 Über die Berührung fester elastische Körper *J. Reine Angew. Math.* **92** 156–71
[34] Crowe C T, Sommerfeld M and Tsuji Y 1998 *Multiphase Flows with Droplets and Particles* (Boca Raton, FL: CRC Press)
[35] Lashkov V A 1992 Drag of a cylinder in a two-phase flow *Fluid Dyn.* **27** 93–7
[36] Fleischmann S T and Sallet D W 1981 Vortex shedding from cylinders and the resulting unsteady forces and flow phenomenon: part I *Shock Vib. Dig.* **13** 9–22
[37] Tsuji Y, Morikawa Y and Shiomi H 1984 LDV measurements of an air-solid two-phase flow in a vertical pipe *J. Fluid Mech.* **139** 417–34
[38] Bohnet M and Triesch O 2003 Influence of particles on fluid turbulence in pipe and diffuser gas-solids flow *Chem. Eng. Technol.* **26** 1254–61
[39] Hetsroni G 1989 Particles-turbulence interaction *Int. J. Multiph. Flow* **15** 735–46
[40] Gore R A and Crowe C T 1989 Effect of particle size on modulating turbulence intensity *Int. J. Multiph. Flow* **15** 279–85
[41] Squires K D and Eaton J K 1991 Preferential concentration of particles by turbulence *Phys. Fluids* A **3** 1169–78